

## Interfacial electronic states of misfit heterostructure between hexagonal ZnO and cubic NiO

Yaping Li,<sup>1,2</sup> Hui-Qiong Wang<sup>①,1,3,\*</sup> Kurash Ibrahim<sup>②,4,†</sup> Jia-Ou Wang,<sup>4</sup> Rui Wu,<sup>4</sup> Hai-Jie Qian,<sup>4</sup> Huanhua Wang<sup>③,4</sup> Tao Lei,<sup>4</sup> Zhiqiang Wang,<sup>1</sup> Xiaojun Li,<sup>1</sup> Meng Wu<sup>④,1</sup> Jin-Cheng Zheng,<sup>1,3</sup> Junyong Kang,<sup>1</sup> Lihua Zhang<sup>⑤,5</sup> Kim Kisslinger,<sup>5</sup> Lijun Wu,<sup>⑥,‡</sup> and Yimei Zhu<sup>6</sup>

<sup>1</sup>Fujian Provincial Key Laboratory of Semiconductors and Applications, Collaborative Innovation Center for Optoelectronic Semiconductors and Efficient Devices, Department of Physics, Xiamen University, Xiamen 361005, People's Republic of China

<sup>2</sup>College of Science, Henan University of Technology, Zhengzhou 450001, People's Republic of China

<sup>3</sup>Xiamen University Malaysia, Sepang 43900, Malaysia

<sup>4</sup>Beijing Synchrotron Radiation Facility, Institute of High Energy Physics, Chinese Academy of Sciences, Beijing 100049, People's Republic of China

<sup>5</sup>Condensed Matter Physics and Materials Science Department, Brookhaven National Laboratory, Upton, New York 11973, USA

<sup>6</sup>Center for Functional Nanomaterials, Brookhaven National Laboratory, Upton, New York 11973, USA



(Received 12 October 2019; accepted 29 October 2020; published 9 December 2020)

The combination of materials with dissimilar symmetries can induce a large amount of stress at the interfacial layer of films, thereby promoting the appearance of novel properties in related devices. The study of the interfacial state is critical for determining the inner mechanism. In this work, the misfit heterostructure between cubic NiO films and wurtzite ZnO is investigated. A NiO film grown using molecular beam epitaxy on a ZnO substrate shows a highly (100)-oriented texture featuring three domains with a rotation angle of 30°, which is in agreement with first principles calculations. Misfit-induced dislocations and lattice distortions within the interfacial layers of the NiO film give rise to interfacial electronic states, which are different from those in bulk; these electronic states are analyzed by *in situ* synchrotron-based x-ray photoelectron spectroscopy, ultraviolet photoelectron spectroscopy, x-ray absorption spectroscopy, and *ex situ* electron energy loss spectroscopy. Additionally, the origin of these interfacial states is discussed. This work aims to provide insights for the integration of semiconducting hexagonal ZnO with other functional materials that have a cubic symmetry. Additionally, we investigate the integration of photon and electron-based techniques to explore the interfacial states of complex interfaces, which is an important aspect of material science.

DOI: [10.1103/PhysRevMaterials.4.124601](https://doi.org/10.1103/PhysRevMaterials.4.124601)

### I. INTRODUCTION

An interfacial electronic structure plays an essential role in modern device fabrications that involve oxide heteroepitaxy because the interfacial electronic structure greatly influences the stability and functions of fabricated devices. Epitaxial interfaces with polar and nonpolar planes have also generated considerable interest because they possess a range of desirable properties for functional devices [1–6]. With dissimilar lattice structures, novel physical phenomena appear at their interface. The stark effect of the polar semiconductor GaN can be decreased by coupling with a cubic substrate, which results in improved quantum efficiency [7]. Bera reported a versatile light-switchable resistive switching memory based on the highly tunable on and off states of a ZnO/NSTO heterojunction with a high and persistent photoconductivity [2]. An interface comprised of such dissimilar materials exhibits a wide range of interesting structural, electronic, and magnetic properties due to the competition of stabilization

mechanisms within the interior of the interfacial layer. The system of a NiO/ZnO heterostructure is studied in this work. Wurtzite ZnO possesses a wide band gap of 3.37 eV and a large exciton binding energy of 60 meV at room temperature, as well as being highly transparent in the visible region; these properties make it appropriate for modern functional devices, such as light-emitting diodes (LEDs), detectors, and optical sensors in the ultraviolet region [8–11]. In contrast, stable *p*-type ZnO thin films have not been very successful because of their self-compensation that is caused by a large concentration of background *n*-type carriers [12,13]; this self-compensation is one of the vital issues to be resolved before promoting their applications in next generation electronics. Therefore, stable *p*-type oxide-based materials, such as NiO, have been studied. As a *p*-type oxide with a high stability and reproducibility, cubic NiO has stable chemical properties, a wide band gap of 3.7 eV, and excellent electrical, optical, and magnetic properties, thereby making it a suitable alternative for *p*-type ZnO. Indeed, a number of *p*-NiO/*n*-ZnO heterojunction-based optoelectronic devices, such as ultraviolet detectors and LEDs, have been fabricated [14–18]. Some studies have investigated the band offset of NiO/ZnO heterojunctions [19–21], but a more detailed exploration of the interfacial electronic structure

\*Corresponding author: [hqwang@xmu.edu.cn](mailto:hqwang@xmu.edu.cn)

†Corresponding author: [kurash@ihep.ac.cn](mailto:kurash@ihep.ac.cn)

‡Corresponding author: [ljwu@bnl.gov](mailto:ljwu@bnl.gov)

of NiO/ZnO heterojunctions is the motivation behind this work.

To probe the interfacial states, photon and electron techniques are combined in this work, i.e., *in situ* synchrotron-based photon techniques are combined with electron techniques to fully explore the interfacial atomic and electronic structure between hexagonal ZnO and cubic NiO. *In situ* photoelectron spectroscopy (PES), including x-ray photoelectric spectroscopy (XPS) and ultraviolet photoemission spectroscopy (UPS), can measure the emergent phenomena at the interface that is controlled by the electronic states localized at the buried interfacial layers by obtaining the electronic states of the core level and valence band [21–24]. In addition, the spatial electronic structure of the conduction band can be obtained by polarization-dependent x-ray absorption spectroscopy (XAS) [25,26]. To directly visualize the ionic displacement with a high spatial resolution to corroborate the x-ray spectroscopy results, electron microscopy is also employed in the interfacial studies [6,22,27–34]. Combined with electron energy loss spectroscopy (EELS), atomic resolution scanning transmission electron microscopy (STEM) provides information on the local electronic structure around an atomic column irradiated by the incident electron probe, which is usually used to probe the interfacial electronic state, such as the metal valence states, holes in the hybridized *p-d* band, and interfacial dislocations, including oxygen vacancies and lattice distortions [28,35]. As a cross-section probe method, STEM and EELS can provide the evolution process from the interface to the bulk material. In this work, the crystal

structure of the NiO film is measured by x-ray diffraction (XRD), and the results of  $\varphi$ -scan XRD provide the epitaxial relationship of the heterostructure.

## II. RESULTS

### A. Epitaxial relationship of the interfaces

Figure 1(a) shows the XRD patterns of the NiO films grown on ZnO (0001), with two featured peaks at approximately 34.4 and 43.4°, corresponding to ZnO (0002) and NiO (002), respectively. The peak of NiO (002) is clearly wider than that of ZnO (0002), and the widening of the NiO diffraction peak may be the combination of the finite thickness (~60 nm) and multiple oriented domains of the NiO epilayer. To determine the epitaxial relationship,  $\varphi$ -scan XRD was performed, as shown in Fig. 1(b). There are six {1-101} peaks separated by 60° in the ZnO  $\varphi$  scan ( $\chi = 61.6^\circ$  and  $2\theta = 36.3^\circ$ ), which is consistent with the sixfold [0001] symmetry of the ZnO crystal. For NiO, four {111} peaks separated by 90° are expected in the  $\varphi$  scan with  $\chi = 54.7^\circ$  and  $2\theta = 37.3^\circ$  based on its fourfold [001] symmetry. The 12 {111} peaks in the  $\varphi$  scan can therefore be divided into three sets of {111} peaks with each set corresponding to an orientation domain that consists of four {111} peaks. Figure 1(c) shows the relationship among the three NiO domains and ZnO substrate in the reciprocal space of the [001]<sub>NiO</sub>/[0001]<sub>ZnO</sub> projection based on the  $\varphi$  scan in Fig. 1(b). From the above, we conclude the following as the relationship among the NiO domains and ZnO substrate:

$$(110)_{\text{NiO-I}} \parallel (10-10)_{\text{ZnO}}, (-110)_{\text{NiO-I}} \parallel (-12-10)_{\text{ZnO}}, [001]_{\text{NiO-I}} \parallel [0001]_{\text{ZnO}}, \quad (1)$$

$$(110)_{\text{NiO-II}} \parallel (01-10)_{\text{ZnO}}, (-110)_{\text{NiO-II}} \parallel (-2110)_{\text{ZnO}}, [001]_{\text{NiO-II}} \parallel [0001]_{\text{ZnO}}, \quad (2)$$

$$(110)_{\text{NiO-III}} \parallel (-1100)_{\text{ZnO}}, (-110)_{\text{NiO-III}} \parallel (-1-120)_{\text{ZnO}}, [001]_{\text{NiO-III}} \parallel [0001]_{\text{ZnO}}, \quad (3)$$

where the subscripts ZnO, NiO-I, NiO-II, and NiO-III represent the ZnO substrate and domains I, II, and III of NiO, respectively.

The observation of three NiO domains is consistent with the six degrees of symmetry along [0001] of the ZnO substrate. Four NiO {110} are equivalent and are the same as six ZnO {1-100}. Therefore, there will be equal probability for NiO to align one of its four {110} to be parallel to one of the six ZnO {1-100}, resulting in the formation of  $N_{RD}$ -independent NiO domains with  $N_{RD} = \frac{lcm(n,m)}{m}$ , where  $N_{RD}$  is the number of rotational domains expected in the grown epilayer;  $n$  denotes the  $C_n$  rotational symmetry of the substrate crystal with rotation angles  $\Phi_i = 2\pi/n$ ;  $m$  denotes the  $C_m$  rotational symmetry of the epilayer crystal with rotation angles  $\Phi_j = 2\pi/m$ ; and  $lcm(n, m) = k/(i/n + j/m)$  is the least common multiple of  $n$  and  $m$ , where  $i, j$ , and  $k$  are integers [36]. In our case, the hexagonal bulk ZnO and cubic-structured NiO films have rotational symmetries of  $C_6$  ( $n = 6$ ) and  $C_4$  ( $m = 4$ ), respectively, and  $lcm(6, 4) = 12$ . Therefore,  $N_{RD} = 12/4 = 3$ , i.e., three rotational domains are expected in the cubic NiO epilayer grown on the

hexagonal ZnO substrate, which is exactly what our results show.

To characterize the interfacial structure, we performed high-resolution transmission electron microscopy (HRTEM) and scanning transmission electron microscopy (STEM) studies on the film. As shown in Fig. S1 of the Supplemental Material, the total thickness of the NiO film is approximately 60 nm [37]. Figures 2(a) and 2(b) shows the STEM images acquired by a high-angle annular dark field (HAADF) detector and viewed along the substrate (a)  $[-12-10]$  and (b)  $[-1100]$  directions, respectively. The bright contrast dots on the left and right correspond to Ni and Zn atoms, respectively. O atoms are invisible due to their low atomic number. The interface between the NiO film and ZnO substrate is sharp. The NiO film consists of domains with a domain size of approximately 4–10 nm in the *ab* plane and tens of nanometers along the *c* direction (nanorod shape). The domain in the middle part, outlined by white dashed lines in Fig. 2(a), shows a centered-rectangle atomic arrangement, which is consistent with the NiO $[-110]$  projection [Fig. 2(c)]. The fast Fourier transform (FFT) (inset) of the image confirms this as it can be indexed as the  $(-110)^*$

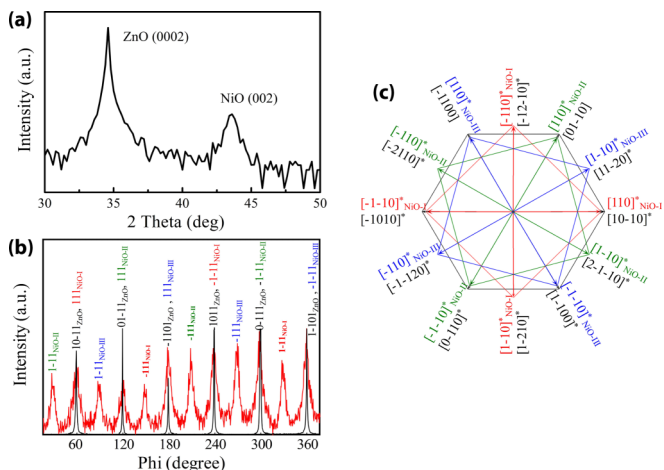


FIG. 1. (a) XRD data shown in a log scale for the grown NiO thin films that show the [001]-oriented texture. The thickness of the NiO films is estimated to be 60 nm from the HRTEM results. (b) High-resolution 0–360°  $\varphi$  scan of the (001) NiO film (red line) on the (0001) ZnO substrate (black line). The  $\chi$  and  $2\theta$  for NiO are 54.7 and 37.3°, respectively, and those for ZnO are 61.6 and 36.3° for ZnO, respectively. The six peaks in the ZnO  $\varphi$  scan (black line) can be indexed as six symmetry related {1-101}. The twelve peaks in NiO  $\varphi$ -scan (red line) can be indexed as three sets of {111}, with each set having four symmetry-related {111} peaks. The subscripts ZnO, NiO-I, NiO-II, and NiO-III represent the ZnO substrate and domains I, II, and III of NiO, respectively. (c) The [001] projection of three NiO orientation domains and the [0001] projection of the ZnO substrate. The red, green, and blue arrows represent projections of reciprocal  $\{111\}^*$  vectors (or the normal of the corresponding {111} plane) of the NiO-I, NiO-II, and NiO-III domains, respectively. The six black arrows represent the six projections of reciprocal  $\{10-11\}^*$  vectors (or the normal of the corresponding {10-11} plane) of the ZnO substrate. The red, green, and blue squares along with the black hexagon represent the (001) plane of the NiO-I, NiO-II, NiO-III domains and the (0001) ZnO plane, respectively.

pattern of rocksalt NiO. The relationship between this domain and the substrate ZnO is the same as that between NiO-I and ZnO, which was determined by the  $\varphi$ -scan XRD pattern [see Fig. 1(b)]. We notice that along this direction, the NiO-II and NiO-III domains are viewed along the high index zone, e.g.,  $[4,15,0]$  for NiO-II and  $[15,4,0]$  for NiO-III, in which the projected distances among the atoms along the vertical direction are too close to be resolved [see the bottom-left part of Fig. 2(e)]. In this case, a streaklike pattern is formed with a spacing of approximately 0.21 nm. We have also simulated the STEM-HAADF image with the beam along the NiO [140] direction, which is just 0.9° off the  $[4,15,0]$  direction (Fig. S2 [37]). The simulation agrees with the observation very well. We further notice that the images viewed along all  $(4, 15, 0)$ , e.g.,  $[4,15,0]$  and  $[15,4,0]$ , are the same due to the cubic symmetry of NiO. Thus, the domains with streaky patterns are either the NiO-II or NiO-III domains in Fig. 2(a). When viewed along the  $[-1100]_{\text{ZnO}}$  direction by tilting the sample 30° around the  $[0001]_{\text{ZnO}}$  axis, the NiO-III domain is in the  $[110]_{\text{NiO-III}}$  zone and exhibits a centered-rectangular atomic arrangement, as shown in the middle part of the domain in Fig. 2(b). In this case, the NiO-I and NiO-II domains are

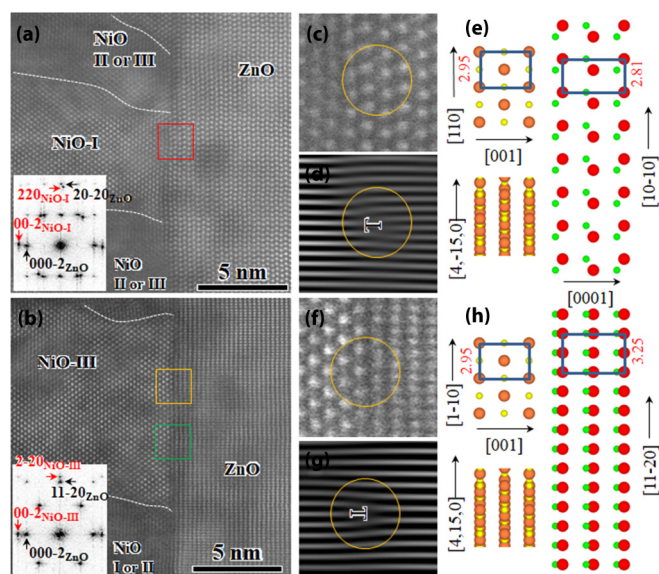


FIG. 2. (a),(b) Cross-section STEM-HAADF images with beams along the (a)  $[-12-10]$  and (b)  $[-1100]$  directions of the ZnO substrate. The white dots on the left and right correspond to Ni and Zn atoms, respectively. O atoms are invisible due to their low atomic number. The insets are the corresponding FFTs of the images. (c),(f) Magnified images from the area outlined by the (c) red and (f) yellow squares in (a) and (b). There is another dislocation in the area marked by a green square. (d),(g) Inverse FFT images of the same area in (c) and (f) by applying an aperture with the (d)  $220_{\text{NiO-I}}/20-20_{\text{ZnO}}$  and (g)  $2-20_{\text{NiO-III}}/11-20_{\text{ZnO}}$  spots of the corresponding FFT (inset) of the STEM-HAADF image in (a) and (b). Dislocations are clearly seen and marked with a T. (e) Projection of NiO  $[-110]$  (top) and  $[-1-40]$  (bottom) along with ZnO  $[-12-10]$ . (h) Projection of NiO  $[110]$  (top) and  $[-4-10]$  (bottom) along with ZnO  $[1-100]$ .

in the high-index zone ( $[-15, 4, 0]_{\text{NiO-I}}$  and  $[-4, 15, 0]_{\text{NiO-II}}$ ) and show streaklike patterns in the image. The relationship observed by STEM images among the NiO domains and ZnO is therefore consistent with the  $\varphi$ -scan XRD results.

To verify the equivalence of the three rotational domains that are observed in the experiment with an angle of 30°, we perform first principles calculations on three rotational models, as shown in Figs. 3(a)–3(c). In the three rotational models, the orientation of the NiO component is fixed. From the corresponding local crystal structures of the top ZnO layer [Figs. 3(d)–3(f)], we can find that model 1 (model 3) can be achieved by a 30° counterclockwise (clockwise) rotation of the ZnO component from model 2. Two cases of the interfacial structure are considered, i.e., without [Fig. 3(g)] and with [Fig. 3(h)] two hexagonal NiO buffer layers embedded at the NiO/ZnO interface. Without and with the hexagonal NiO buffer layers, the formation energy of the three rotational models can be defined as

$$E_{\text{form}} = E(\text{NiO/ZnO}) - E(\text{ZnO})_{\text{wurzite}} - E(\text{NiO})_{\text{rocksalt}} \quad \text{and} \\
 E_{\text{form}} = E(\text{NiO/ZnO}) - E(\text{ZnO})_{\text{wurzite}} - E(\text{NiO})_{\text{rocksalt}} \\
 - E(\text{NiO})_{\text{wurzite}},$$

respectively, where  $E(\text{NiO/ZnO})$ ,  $E(\text{ZnO})_{\text{wurzite}}$ ,  $E(\text{NiO})_{\text{rocksalt}}$ , and  $E(\text{NiO})_{\text{wurzite}}$  are the total energy of

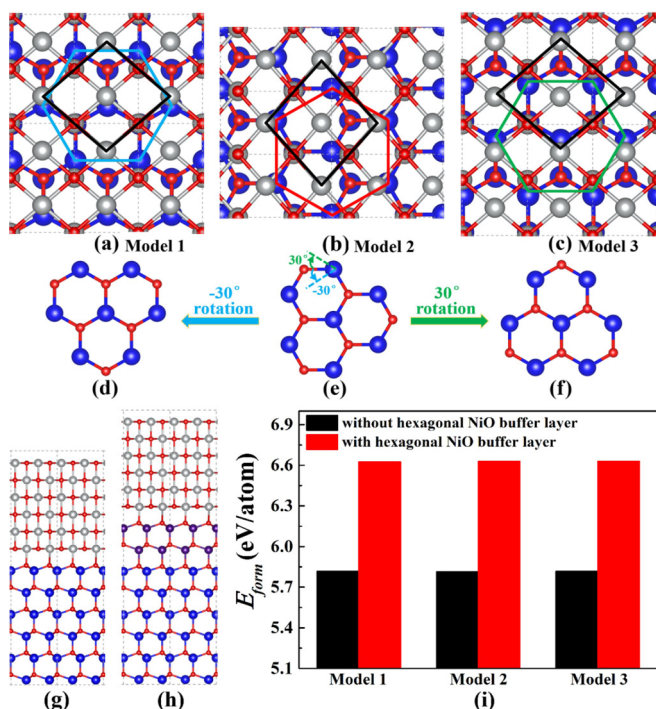


FIG. 3. (a)–(c) The top views of the crystal structures of the three rotational models. The orientations of NiO and ZnO are marked by a black quadrilateral, and blue, red, and green hexagons. (d)–(f) Corresponding local crystal structures of the top ZnO layer. In the three rotational models, the orientation of the NiO component is fixed, and model 1 (model 3) can be achieved by a  $30^\circ$  counterclockwise (clockwise) rotation of the ZnO component from model 2. (g),(h) Side views of the crystal structures of the NiO/ZnO superlattice models without and with the hexagonal NiO buffer layer, respectively. The large blue and gray balls and the small red balls represent the Zn, Ni, and O atoms, respectively. The large purple balls represent Ni atoms in the hexagonal NiO buffer layer. (i) Formation energy of the three rotational models with/without the hexagonal NiO buffer layer.

the NiO/ZnO superlattice, wurtzite ZnO, rocksalt NiO, and wurtzite NiO, respectively.

As seen from Fig. 3(i), the formation energy difference among the three models without hexagonal NiO buffer layers is less than 4 meV/atom, indicating that the three rotational models are equivalent. Furthermore, the formation energy difference among the three models with hexagonal NiO buffer layers remains less than 4 meV/atom. Both the symmetry of the crystal structure and the formation energy verify the equivalence of the three rotational domains.

*Lattice coupling between the film and substrate.* The  $d$  spacings of NiO (002) and (220) are measured to be  $2.08 \pm 0.01$  and  $1.48 \pm 0.01$  Å, respectively, from the NiO 002 and 220 spots in the FFT results of the image containing both NiO and ZnO, e.g., the insets in Figs. 2(a) and 2(b) with ZnO 0002, 20-20, and 11-20 as references. These are basically the same as the corresponding  $d$  spacing of the bulk NiO, indicating a fully relaxed NiO thin film. The lattice mismatch between the film and the substrate is therefore calculated to be 5% along the  $[10-10]_{\text{ZnO}}$  direction and 9.2% along the  $[11-20]_{\text{ZnO}}$  direction. To exam the dislocations expected to accommodate

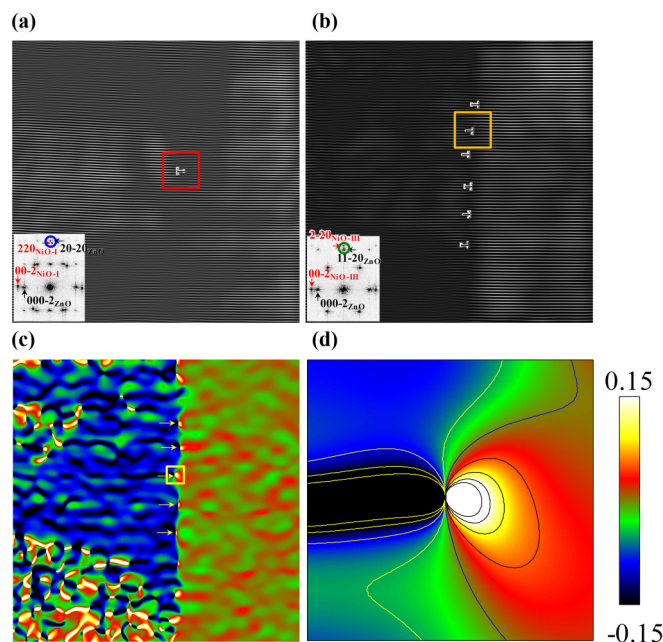


FIG. 4. Panels (a) and (b) are inverse FFT images obtained by applying an aperture with the  $220_{\text{NiO-I}}/20-20_{\text{ZnO}}$  and  $2-20_{\text{NiO-III}}/11-20_{\text{ZnO}}$  spots of the FFT in the STEM-HAADF image in Figs. 2(a) and 2(b), respectively. Horizontal fringes with spacing of approximately 1.48 Å for the NiO-I domain and 1.41 Å for ZnO in (a) and 1.48 Å for the NiO-III domain and 1.63 Å for ZnO in (b). One dislocation is present in (a), while six dislocations with a spacing of approximately 1.6 nm are seen in (b) and as marked with a  $T$ . Panels (c) and (d) are the in-plane strain ( $\epsilon_{xx}$ ) maps of the interfaces with  $x$  along ZnO  $[11-20]$  and the enlarged view from the marked area in (c).

the lattice mismatch, horizontal fringe images were obtained by applying an aperture in the  $220_{\text{NiO-I}}/20-20_{\text{ZnO}}$  and  $2-20_{\text{NiO-III}}/11-20_{\text{ZnO}}$  spots of the FFT in the STEM-HAADF images (Fig. 2). There are “ $T$ ” type dislocations in the NiO film at the interfacial layers, which point in opposite directions, as shown in Figs. 2(d) and 2(g). This dislocation is caused by the difference in the horizontal fringe spacings of NiO and ZnO, i.e., approximately 1.48 Å for the NiO-I domain and 1.41 Å for the ZnO substrate [Fig. 4(a)], as well as 1.48 Å for the NiO-III domain and 1.63 Å for the ZnO substrate [Fig. 4(b)]. One dislocation is present in Fig. 4(a), while six dislocations with a spacing of approximately 1.6 nm are seen in Fig. 4(b), and these dislocations are marked with a “ $T$ ”. From the fringe images, the dislocation Burger’s vector is determined to be  $\frac{1}{4}\langle 110 \rangle$ . The spacing of the dislocations is therefore calculated to be 2.96 nm along  $[10-10]_{\text{ZnO}}$  and 1.63 nm along  $[11-20]_{\text{ZnO}}$ , which is consistent with the dislocations observed in the fringe images.

The strain mapping of  $\epsilon_{xx}$  [Fig. 4(c),  $x$  along  $[11-20]_{\text{ZnO}}$ ] shows large, interconnected areas of weak, strained areas. Deep valleys (blue) are the highly compressed region with a compressive strain of  $\epsilon_{xx} \cong -0.15$ , whereas sharp peaks (yellow) are the highly stretched region with a tensile strain of  $\epsilon_{xx} \cong 0.15$ . The enlarged view of the area marked by the white rectangle in Fig. 4(c) is displayed in Fig. 4(d). In this enlarged image, the yellow and blue lines mark the negative

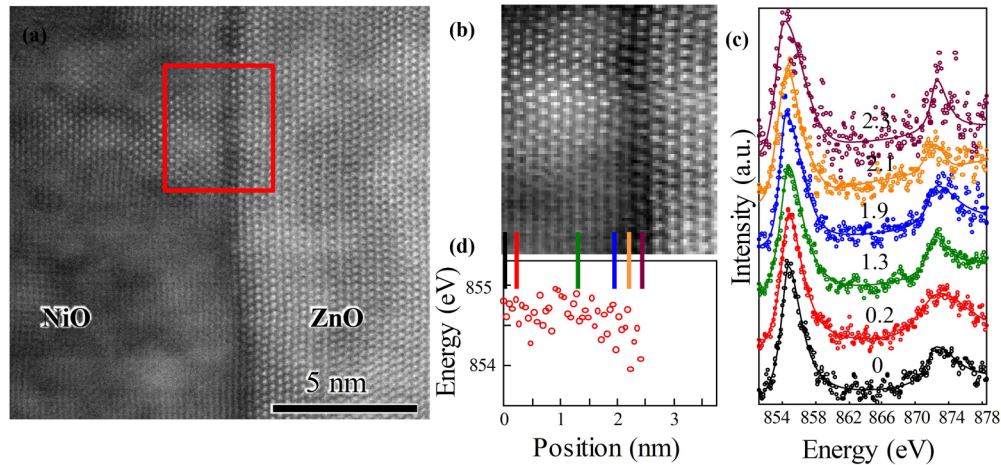


FIG. 5. (a) STEM-HAADF survey image with a beam along the  $[-12-10]$  direction of the ZnO substrate. The rectangle marks the area for the EELS spectrum image. (b) Simultaneously, acquired STEM-HAADF image during the acquisition of the 2D EELS spectrum image. (c) Ni  $L_{3,2}$  edges (dots) by averaging vertically in the EELS spectrum image at several positions indicated by the vertical lines of the same color in (b). The solid lines are refined curves using a combination of asymmetric Gaussian and Lorentzian functions. (d) Refined Ni  $L_3$  edge energy as a function of position. The Ni  $L_3$  energy drops at the interface.

and positive strains, respectively. Thus, in the NiO film close to the interface, the strain displaced in the strain map for the  $\epsilon_{xx}$  component is considered to be caused by the misfit between the overlayer and the substrate. This strain is periodically released through the formation of dislocations at the interface, as indicated by the yellow arrows in Fig. 4(c). Furthermore, these dislocations are uniformly distributed along the interface.

## B. Electronic structure at the interfaces

### 1. Conduction band structure at the interface

We studied the electronic structure at the interfaces by first performing STEM-EELS analyses, which are very useful for investigating the electronic structures at the nanometer scale with a high spatial resolution, especially at interfaces where the charge distribution changes locally within several nanoscales [6,31,32,38]. The Ni  $L_{3,2}$  and O  $K$  edge spectra correspond to transitions from Ni  $2p$  to Ni  $3d$  and from O  $1s$  to O  $2p$ , respectively. We focused on the fine structure of the Ni  $L$  and O  $K$  edge spectra because they are both sensitive to the hybridized  $3d^8$  band of NiO [39]. As shown in Fig. 5, when viewed along the ZnO  $[-12-10]$  direction, a two-dimensional (2D) EELS spectrum image with Ni  $L_3$  and  $L_2$  edges was acquired across the interface, and this is marked by the red rectangle in Fig. 5(a). The energy of the EELS spectra was calibrated by the simultaneously acquired zero loss spectra. To improve the signal-to-noise ratio, the 2D spectrum image was averaged vertically to a 1D spectrum image across the interface. Figure 5(c) shows the spectra at several positions, and the color of these data are the same as the vertical guide lines in Fig. 5(b). The numbers in Fig. 5(c) denote the distance to the left of the rectangle, which means the bottom black spectrum that originates from the NiO bulk and the uppermost brown spectrum that originates from the NiO layers at the interface. The solid lines are refined curves using a combination of asymmetric Gaussian and Lorentzian functions (as shown in Supplemental Material Eq. (1) [37]). Figure 5(d)

shows the refined Ni  $L_3$  peak energy as a function of the position. The peak shape broadens at the interface. As electrons at the Ni  $2p$  level are ejected into the empty/unoccupied valence states, the energy loss reflects the distribution of the unfilled states. Additionally, this broadening effect indicates that there are changes in the NiO electronic structure at the interface, e.g., lattice distortions caused by the interfacial strain exist in the NiO overlayer at the interface, which contributes to the broadening of the peak.

Figure 6(b) is the STEM-HAADF survey image with a beam along the  $[-12-10]$  direction of the ZnO substrate. The red line across the interface marks the scan line (position from 0 to 17 nm). A 1D EELS image of the O  $K$  and Ni  $L$  edges was acquired along the red line, indicated in Fig. 6(b), that ran across the interfacial region shown in Fig. 6(a). The sharp termination of the Ni  $L$  edges indicates a sharp interface. In the upper part of Fig. 6(c), the O  $K$  edges, obtained by vertically averaging the spectra marked by the black and red rectangles in Fig. 6(a), originate from NiO and ZnO, respectively [6,39]. In the lower part of Fig. 6(c), the black and red circles, representing the percentage of NiO and ZnO, change as a function of position (from NiO to ZnO), as calculated from the black and red rectangles in Fig. 6(a); the results are based on a multiple linear least square (MLLS) fitting with the reference spectra on top. An example of MLLS fitting for the NiO/ZnO interface is shown in Fig. S3 [37]. The blue line shows the simultaneously acquired STEM-HAADF image intensity during the acquisition of the 1D EELS spectrum image. A decrease in the oxygen content of the interfacial layers ( $\sim 1.7$  nm) can be distinguished, which indicates oxygen defects in the interfacial layers of NiO.

Analogous to the EELS, XAS was measured at a synchrotron, which is more sensitive to the surface states and is able to provide information on the electronic states, combined to study the atomic bonding and electronic structures at the interface. Ni  $L_{3,2}$  edge absorption spectra were measured in the total electron yield (TEY) mode, as shown in Fig. 7. Figures 7(a) and 7(b) show the polarization-dependent Ni  $L_{3,2}$

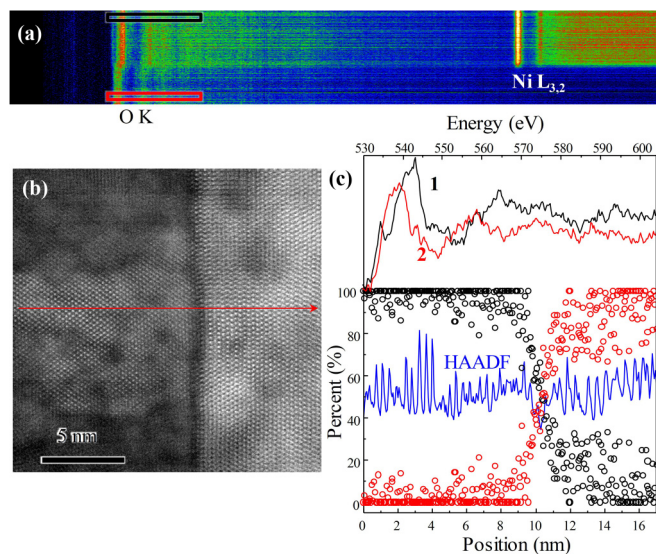


FIG. 6. (a) 1D EELS spectrum image for O K and Ni  $L_{3,2}$  edges from the scan line shown in (b). (b) STEM-HAADF survey image with a beam along the  $[-12-10]$  direction of the ZnO substrate. (c) Upper part: O K edges by vertically averaging the spectra marked by black and red rectangles in (a); the axis is labeled at the top. These two spectra represent the O K edge in the NiO film and ZnO substrate, respectively. The spectra are used as the reference spectra for multiple linear least square (MLLS) fitting. Lower part: Percentage contribution of the O K edge in the NiO film (black dots) and ZnO (red dots) as a function of position [from NiO to ZnO, as indicated by the red arrow in (b)] calculated from the EELS spectrum in (a), which is based on the MLLS fitting with two reference O K spectra at the top. The position is labeled at the bottom. The STEM-HAADF image intensity simultaneously acquired during the EELS acquisition is included as the blue line.

XAS spectra of NiO films at different deposition times. The angle between the light and the sample surface is provided

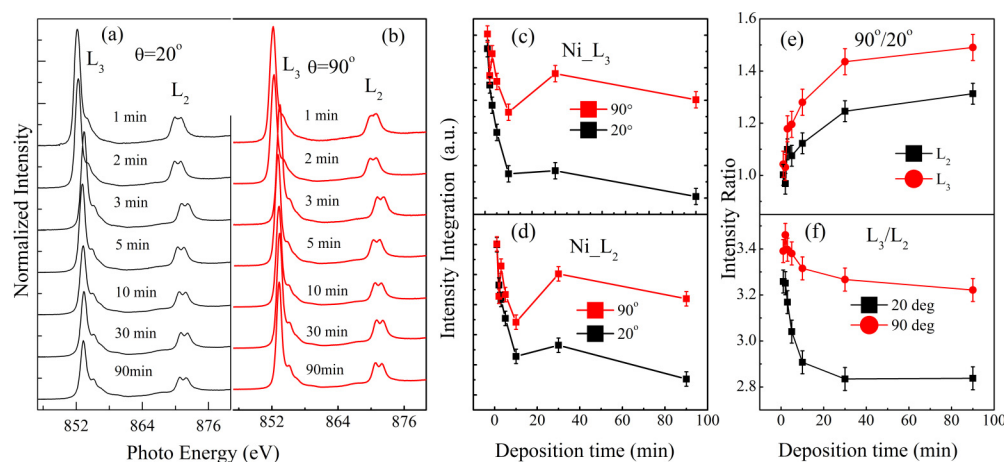


FIG. 7. Panels (a) and (b) are experimental polarization-dependent Ni  $L_{3,2}$  XAS results of the NiO films at different deposition times.  $\theta$  is the angle between the light and the sample surface ( $\theta = 90^\circ$  means normal light incidence). Panels (c) and (d) are the integrated intensities of the Ni  $L_3$  and  $L_2$  peaks for different deposition times at  $20^\circ$  (black square) and  $90^\circ$  (red circle), respectively. Panel (e) is the relative integrated intensity ratio from the incident angles at 90 vs  $20^\circ$  as a function of the deposition time, which is calculated from the Ni  $L_3$  (black) and Ni  $L_2$  edges (red), respectively. Panel (f) is the relative integrated intensity ratio from the absorption edges at Ni  $L_3$  versus  $L_2$  as a function of the deposition time, which is calculated from the incident angles at  $90^\circ$  and  $20^\circ$ , respectively.

by  $\theta$  ( $\theta = 90^\circ$  means normal light incidence with an electric field vector  $\vec{E}$  lying in the plane of the crystal). Two angles were chosen,  $20^\circ$  and  $90^\circ$ , which preferred the in-plane and out-of-plane orientations, respectively. The spectra were first normalized to  $I_0$ , followed by the subtraction of the pre-edge line background and then the peak intensity at 880 eV was normalized to 1. The general line shape of the spectra is very similar to that of thicker NiO films and bulk NiO [40]. The Ni  $L_3$  absorption edge is found to shift toward lower energy for the interfacial layers. The shift of the absorption edge means a decrease in the oxidation of NiO, which is the result of oxygen defects at the interface [41,42]. There are satellite peaks near the major peak, and the major peak in the Ni  $L_3$  spectra is due to the transitions from  $2p^63d^8$  to  $2p^53d^9$ , while the satellite peaks near the major peak are derived from the multiplet splitting effect, which results from the interplay between the hybridization and Coulomb repulsion [43]. In bulk NiO, the satellite peaks are the result of a mixture of  $2p^63d^9L$  and  $2p^63d^{10}L^2$  ground states ( $L$  denotes a hole in the ligand for O atoms) [43,44] and multiple transition processes of  $p-d$  and  $d-d$  transitions [45]. As seen in Figs. 7(a) and 7(b), the satellite peak intensities at 1 min are much weaker than those at 90 min, indicating a relatively weak hybridization between Ni  $3d$  and O  $2p$  and a relatively weak correlation among the Ni  $3d$  electrons at the initial growth stages.

The integrated areas of the Ni  $L_3$  peak for different deposition times at  $20^\circ$  (black square) and  $90^\circ$  (red circle) are shown in Fig. 7(c), and the absorption intensity of Ni  $L_3$  increases when close to the interface. An increase in unoccupied states is expected in the Ni  $3d$  energy levels of the first few layers of NiO, which will increase the intensity of absorption. With increasing deposition time, a decreasing trend can be clearly seen at both  $20^\circ$  and  $90^\circ$ , indicating an increase in the absorption intensity when closer to the interface and a decrease in the electron occupation of the Ni  $3d$  energy levels. As shown in Fig. 7(e), the relative intensity of  $90^\circ/20^\circ$  decreases when

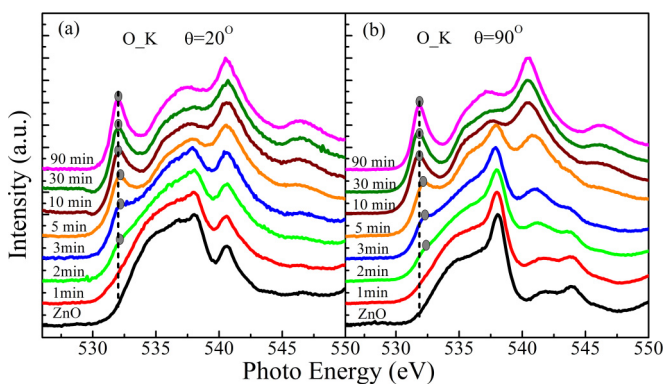


FIG. 8. Experimental O  $1s$  XAS of NiO films at different deposition times with incident angles of  $20^\circ$  (a) and  $90^\circ$  (b).

moving closer to the interface, which means an increase in the electronic occupation of the  $xy$  plane relative to the  $z$  plane at the interface. A similar phenomenon is also observed at the Ni  $L_2$  edge.

The polarization-dependent O  $_K$  absorption spectra, as shown in Fig. 8, also demonstrate the clear evaluation of the conduction band structure as the thickness of the NiO film increases. A new absorption peak originating from the O  $2p$ -Ni  $3d$  hybridization arises at 532 eV when NiO is deposited on the substrate. In addition, this absorption position shifts to a higher energy value at the interfacial layers ( $\theta = 90^\circ$ ), indicating that the charge transfer energy, which is sensitive to the ion coordination of NiO, changes at the

interface [46]. From the STEM results, there exists a series of dislocations at the interface, which can lead to the distortion of the NiO crystal structure at the interface and further shift the absorption edge in the O  $_K$  edges to a higher energy value at  $90^\circ$ , while remaining nearly constant at  $20^\circ$ . The peak at 532 eV broadens during the initial growth stage, indicating crystal field splitting, which is consistent with previous reports [47].

## 2. Valence band structure at the interface

Figure 9 shows the core-level XPS at the different deposition stages by a synchrotron light source (here, incident light energy at 500 eV was chosen for the best resolution). The detailed XPS spectra of Zn  $3p$  for the studied NiO/ZnO samples are shown in Fig. 9(a). The intensity of the main Zn  $3p$  peak decreases with an increasing deposition time of NiO due to the expected attenuation caused by the deposited NiO layer. Following the procedure in Ref. [28], the attenuation of the Zn  $3p$  signal is used to determine the thickness ( $d$ ) of the deposited NiO layer according to the formula

$$d = -\lambda \times \ln\left(\frac{I}{I_0}\right), \quad (4)$$

where  $I_0$  and  $I$  are the spectral intensities of the Zn  $3p$  substrate line before and after the NiO deposition, respectively, and  $\lambda$  is the inelastic mean free path (IMFP) of the Zn  $3p$  photoelectrons in NiO. This model assumes that the NiO layers homogeneously cover the smooth ZnO substrate because it only gives a nominal (i.e., effective) thickness for NiO layers in other morphologies (e.g., island formation). In our case,  $\lambda$  is estimated to be 0.92 nm (using the IMFP values calculated

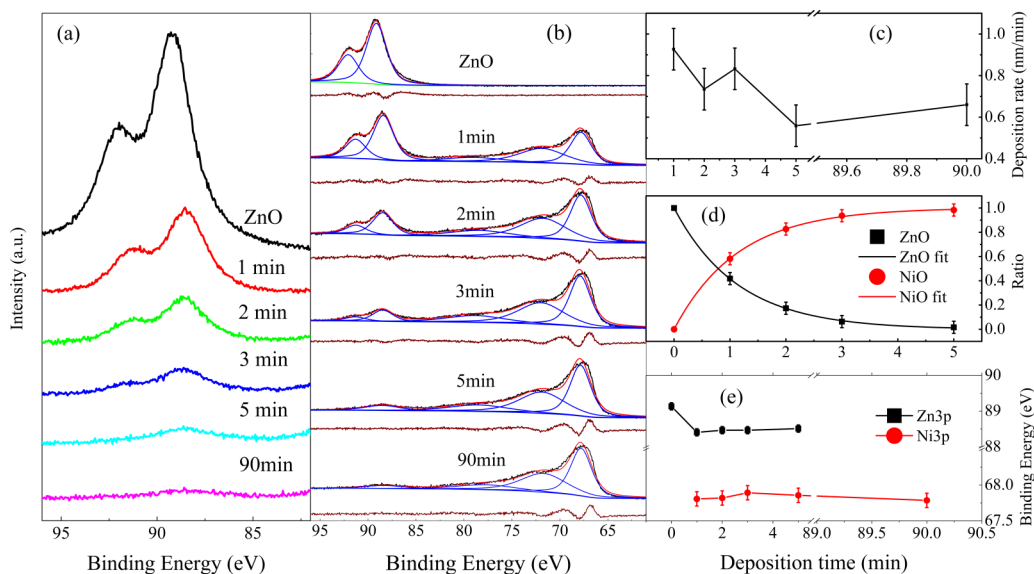


FIG. 9. (a) Synchrotron light source-excited Zn  $3p$  XPS spectra of the cleaned ZnO substrate and NiO/ZnO samples with an incident light energy of 720 eV, for which NiO layers have been deposited by MBE onto ZnO substrates with different deposition times (1–90 min). The spectra are vertically offset for clarity. (b) Fits of the Zn  $3p$  and Ni  $3p$  XPS spectra of the cleaned ZnO substrate and the NiO/ZnO samples grown for 1, 2, 3, 5, and 90 min. For easier comparison, the spectra and respective component fits are vertically offset. Each fit consists of a Shirley background and multiple Voigt profiles to describe Ni  $3p$  and Zn  $3p$ . The residuals (i.e., the difference between data and fit) are also shown. The XPS-derived NiO deposition rate is displayed in panel (c). Panel (d) shows the relative intensity of the ZnO substrate and NiO epitaxial film vs the NiO thickness, which is calculated from the attenuation of the Zn  $3p$  signals via formula (1). The solid curves are calculated by  $I(\text{Zn}3p) = \exp(-d/\lambda)$  and  $I(\text{Ni}3p) = 1 - \exp(-d/\lambda)$ , respectively, where  $d$  is the thickness of the NiO film (main text for details). Panel (e) shows the positions of the Zn  $3p_{3/2}$  and Ni  $3p$  binding energies as a function of the NiO thickness.

TABLE I. Equivalent thicknesses of the epitaxial layer vs the deposition time.

Deposition time (min)	Thickness of epitaxial layers (nm)
1	0.93
2	1.66
3	2.49
5	3.61
10	6.91
30	20.11
90	60.00

by the QUASES-IMFP-TPP2M code developed by Tougaard [48,49]).

The feature Zn 3*p* peak can be decomposed into two sub-peaks: one at 92.1 eV and the other at 89.2 eV. These two peaks seem to entirely disappear after NiO growth for 5 min, and instead, a small portion of the peak appears; this result originates from the NiO satellite rather than the ZnO substrate [50]. As shown in Fig. 9(b), both Zn 3*p* and Ni 3*p* are fitted by Voigt (mixed Lorentzian-Gaussian) functions. The thickness of the NiO epitaxial layer can be obtained by the intensity of Zn 3*p* following the upper formula at the initial deposition stage. However, XPS is surface sensitive, and 95% of the information comes from a thickness less than 3λ, which is ~2.76 nm. The deposition rate of NiO was derived by XPS for thinner films (≤5 mins) and by TEM (as shown in Fig. S1 [37]) for thicker films. The thickness of films with deposition times of 10 and 30 min is estimated from this deposition rate and is shown in Table I. The thickness values in the table are equivalently estimated because the NiO films are not uniformly distributed on the surface of the substrate, especially after only 1 min.

The satellite peak of NiO overlaps with Zn 3*p* and is subtracted from the Zn 3*p* signals at the initial deposition stage. Here, this effect is carefully removed by proportional deduction, i.e., we derive the ratio of this small peak to the main NiO 3*p* peak at 90 min, and then the same ratio is used for those at 1, 2, 3, and 5 min. The relative intensities of the Zn3*p* and Ni3*p* signals are expressed as  $Zn3p(Ni3p)/(Zn3p + Ni3p)$ , which shows an exponential attenuation with the increasing thickness of NiO. As shown in Fig. 9(d), the black square points and red circle points denote the results calculated by the experimental data for ZnO and NiO, respectively; the black and red curves are the fitted data by the functions  $I(Zn3p) = \exp(-d/\lambda)$  and  $I(Ni3p) = 1 - \exp(-d/\lambda)$ , respectively, where  $d$  is the thickness of NiO and  $\lambda$  is the IMFP, as mentioned above. The fitting results are in good agreement with the calculated relative intensities, indicating that the method used to calculate the film thickness and deposition rate in this work is reasonable.

As shown in Fig. 9(e), after the growth of the NiO films, an energy shift of 0.7 eV toward a lower binding energy occurs at 1 min compared to the Zn 3*p* spectra of the ZnO substrate. This result is attributed to interface-induced band bending, with the bands of the ZnO substrate moving upward toward the NiO/ZnO interface. A common mechanism is that binding energy (BE) shifts are accompanied by charge transfers. A

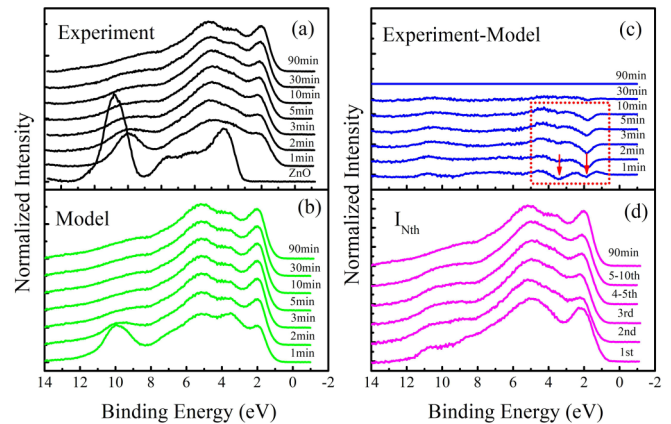


FIG. 10. (a) Experimental UPS spectra of NiO films with different thicknesses grown on ZnO. An inelastic Li-Henrich background has been subtracted from the experimental spectra. Panel (b) shows the UPS spectra using model 1 and calculated via Eq. (5) (the energy position of Zn 3*d* at the ZnO substrate shifts by 0.8 eV to a lower binding energy to align with the Zn 3*d* after the deposition of NiO). Panel (c) shows the different spectra taken by subtracting the calculated spectra of model 1 from the measured spectra. Panel (d) shows the sequential differences taken from (a) using Eq. (6). The intensity has been normalized to have the same integrated area.

shift to a higher BE, i.e.,  $\Delta BE > 0$ , indicates that an atom with a large BE has a more positive or less negative effective charge, while a shift to a low BE, i.e.,  $\Delta BE < 0$ , indicates that an ionized atom has a more electronic charge and its effective charge is either less positive or more negative [51]. Adding an electron to the outermost valence shell leads to a core-level BE shift to lower energy, which decreases the potential felt by the core electron and leads to a shift in the core-level energy [52]. Therefore, the shift in the Zn 3*p* binding energy to a lower energy reveals the presence of more electronic charge. The final state screening effect of the core hole is also a remarkable effect to decrease the binding energy of Zn 3*p* [51,53].

*In situ* synchrotron radiation UPS was used to investigate the electronic structure in the valence band. Figure 10(a) shows the experimental UPS spectra of NiO at different deposition stages with an incident photon energy of 36.2 eV. In addition, the valence band was also measured with a photon energy of 40.8 eV (the same excitation energy from He-ion line radiation, which is commonly used in laboratory UPS) for use in comparisons, and the main shapes of the spectra at 40.8 eV are basically the same as that at 36.2 eV. Inelastic scattering is accounted for by subtracting the Li-Henrich background in Fig. 10(a) [54–56].

The main features of ZnO and NiO are located in the energy range of 1–12 eV. Multiple characteristic peaks can be seen in the valence band spectra for the ZnO substrate, where the peak at 3.1–5 eV is mainly from O 2*p*, the peak at 7.5 eV comes from the hybridization of O 2*p* and Zn 3*d*<sub>4s</sub>; additionally, the strong peak at 10.8 eV is attributed to Zn 3*d*. These features start to show changes after the deposition of NiO (even after only 1 min). A visible shift appears for Zn 3*d*, as well as for Zn 3*p*. The peak at 4 eV for ZnO is mixed with other electronic states as NiO is deposited, and

the NiO feature appears at 2 eV below the Fermi level; this result comes from the hybridization between Ni 3*d* and O 2*p*, as reported in previous literature [57–60]. In this work, the evolution behavior of the interfacial electronic states will be discussed in detail by using mathematical models. Our experimental spectra reveal clear differences at 1–5 eV below the Fermi level for the NiO films after deposition times of 1–10 min, whereas the difference between the spectra taken at 30 and 90 min is negligible. From the experimental spectra, the spectrum corresponding to 30 min is similar to that at 90 min, but a clear difference is observed at 1–5 eV below the Fermi level for NiO films deposited from 1 to 10 min. Two different models can be used to examine the interfacial density of states from the experimental UPS spectra [24,55,56]:

$$I(d) = I_0^{\text{ZnO}} \exp(-d/\lambda) + I_0^{\text{NiO}} \{1 - \exp[(-d/\lambda)]\}. \quad (5)$$

Equation (5) can be applied to simulate model spectra assuming the interface is abruptly sharp with no interfacial state. Using the ZnO substrate and the 90-min NiO film as the bulk signals for  $I_0^{\text{ZnO}}$  and  $I_0^{\text{NiO}}$ , respectively, the obtained model spectra are shown in Fig. 10(b). Actually, after 3 min of growth (2.97 nm thick), 95% of the signal from the epitaxial layer and the contribution from the substrate can be ignored. The incident photo energy in the UPS measurement is 36.2 eV, and the probing depth is smaller than that in XPS, therefore the value of  $\lambda$  is chosen to be 0.7 nm in this model. To compare the difference between the experimental and model spectra, model spectra were subtracted from the measured spectra of the 1–10 min deposition times, as shown in Fig. 10(c); red arrows are used to show major differences in the energy range of 1–5 eV. For the NiO film with a deposition time of 1 min, two different features of the Ni 3*d* state become evident at 2 and 3.7 eV, compared to that of bulk NiO. The peak at 2 eV comes from Ni 3*d*, so the decrease in this peak means a charge transfer at the interface with an electron transfer from NiO to ZnO. The peak at 3.7 eV is the result of a nonlocal screening effect in NiO, while this effect is greatly reduced for the 1-min deposition because of the broken octahedral symmetry at the interface [52,60,61]. The decrease in the 3.7-eV peak almost disappears after 2 min of growth, but the intensity of the 2-eV peak continues to decrease until 30 min of deposition.

The electronic states at the valence band for the NiO film during the initial deposition stages are different from those of the bulk NiO, and a constant change occurs as the thickness of NiO increases. The development of the interfacial electronic structure can be obtained by taking sequential differences of the experimental UPS spectra as each additional overlayer is deposited on ZnO using the following equation [55]:

$$I_{(j-i)\text{th}} = I_j - I_i \exp(-d_{(j-i)\text{th}}/\lambda), \quad (6)$$

where  $I_i$  denotes the intensity of the sample that is  $i$  nm thick (if the thickness of the epitaxy film is 0 nm, then it means the substrate),  $I_j$  denotes the intensity of the sample that is  $j$  nm thick,  $I_{(j-i)\text{th}}$  is the signal intensity generated from the films of  $(j-i)$  in nm, and  $d_{(j-i)\text{th}}$  denotes the thickness of  $(j-i)$  in nm. Suppose an epilayer with a thickness of  $(j-i)$  nm is deposited after an  $i$ -nm NiO film has been deposited on the substrate. The electronic structure of the  $(j-i)$ th film thickness  $I_{(j-i)\text{th}}$  can then be determined by subtracting the total intensity of  $I_i$ , which is corrected for the attenuation by

the thickness of the  $(j-i)$ th overlayers  $d_{(j-i)\text{th}}$ . The resultant spectra of the NiO overlayers deposited after the first, second, and third mins are shown in Fig. 10(d). For the deposition of 5–10 min, the thickness exceeds the electron mean free path for UPS, hence the layer feature is nearly the same as that in Fig. 10(a). A different state also appears with the interfacial electronic structure at 1.5–5 eV, with relatively few electronic states at the valence band maximum and a decrease in the nonlocal screening effect compared to those of bulk NiO. These observations are similar to those from the comparison of the experimental and model spectra. In Fig. 10(d), there is little difference in the spectral line as the deposition time exceeds 2 min; thus, an interfacial state is confirmed at the interface of NiO/ZnO, which extends up to  $\sim 1.7$  nm into the NiO films. The most significant interfacial state originates from the Ni-O hybridization of the Ni 3*d* electronic state and the interfacial charge transfer between NiO and ZnO with the electron transfer from NiO to ZnO.

### III. DISCUSSION

When a cubic NiO film is epitaxially grown on a wurtzite ZnO substrate, a series of  $T$  type dislocations exist at the interface of the nonpolar NiO and polar ZnO, and the misfit at the interface is reported to be relaxed by forming dislocations at this interface. From the EELS results, oxygen vacancies are determined to be present at the interface, which is a common way to alleviate the misfit at the interface and promote the formation of dislocations at the interface [22,33,34]. The strain in the NiO epitaxial layers leads to NiO lattice distortion around the center of the dislocations while the charge distribution around the Ni sites is distorted by nonuniform Ni-O bond lengths, which induces an interfacial electronic structure. With lattice distortion at the interface, the crystal field around the Ni atoms changes at the interface with a small amount of conduction band splitting. As a result of the oxygen defects and crystal field effects at the interface, the Ni  $L_3$  peak broadens and shifts to a lower energy at the interface in the EELS spectra and the absorption peak in the Ni- $L_3$  edge shift in the XAS spectra. Both the decrease in the satellite peak intensity of the Ni  $L_3$  peak in XAS and the decrease in the intensity of the valence band in UPS indicate the weakened hybridization of Ni 3*d* and O 2*p* at the interface. Thus, oxygen vacancies at the interface can decrease the hybridization between Ni 3*d* and O 2*p*. Interfacial charge transfer is also determined to occur in this system with an electron transfer from NiO to ZnO, which leads to a shift in the binding energy of core-level electrons.

### IV. CONCLUSIONS

In conclusion, by analyzing the interfacial structure between NiO and ZnO, a cubic structure of NiO was grown along the [001] direction on hexagonal ZnO (0001), even with the existence of a large mismatch. Three rotational domains with an angle of 30° were confirmed with the deposited NiO films by phi-scan XRD. DFT and HRTEM were employed to study the atomic interfacial structure. The evaluation of the conduction band, valence band, and core-level structures at the interface between the NiO films and ZnO substrate was

investigated by *in situ* XAS and PES. Gradually different interfaces were proposed by analyzing the evolution of the UPS spectra from the initial deposition of NiO, and the interfacial valence band electronic states, which were identified by comparing the experimental spectra to model spectra. Multi-interfacial states were determined, including the weakening of Ni-O hybridization, crystal field splitting effect in NiO, and charge transfer at the interface. These interfacial electronic states are closely related to the lattice coupling of interfacial layers. This work demonstrates the possibility for integrating functional materials between cubic and hexagonal structures and serves as an example to thoroughly examine the interfacial electronic structure by combining electron and photon techniques.

## V. EXPERIMENTAL METHODS

Before the growth of NiO films, O-terminated ZnO substrates were first cleaned ultrasonically in acetone and subsequently in ethanol before being inserted into an ultrahigh-vacuum system. The surfaces of the substrates were bombarded for 1 h with 600 eV Ar<sup>+</sup> ions to remove the oxygen and carbon contaminations followed by 1 h of annealing at 600 °C at an oxygen pressure of  $1 \times 10^{-5}$  torr. With several cycles of bombardment and annealing, the ZnO surface exhibited clear LEED patterns (not shown here) without reconstruction. Ultrathin NiO overlayers were grown by evaporating Ni on the ZnO surface at an oxygen pressure of  $2 \times 10^{-5}$  torr and at room temperature; the samples were then transferred to the analysis chamber for electronic structure characterization by synchrotron-based XPS, UPS, and XAS measurements. Such a process was carried out seven times with accumulative deposition times of 1, 2, 3, 5, 10, 30, and 90 min. The growth of the NiO film and these *in situ* XPS, UPS, and XAS measurements were carried out at beamline 4B9B of the Beijing Synchrotron Radiation Facility (BSRF), and the crystal structure was examined by *ex situ* synchrotron radiation XRD at beamline 1W1A of the BSRF. *In situ* XAS spectra were collected with linearly polarized light (~80%) from the elliptical electromagnetic wiggler in the total electron yield (TEY) mode. *In situ* synchrotron-based XPS and UPS were performed using incident energies of 500 and 36.2 eV, respectively, at an incident angle of 6.75° (normal detection) to obtain spectra of the core levels (CLs) of Zn 3*p* and Ni 3*p* and the valence band (VB) structures, respectively. The instrument work function and incident energy were both calibrated by the Au Fermi level, and all the spectra were corrected by the Au 4*f* or Au Fermi level. The deposition rate of the NiO film was determined from XPS measurements, after considering the XPS attenuation of the Zn 3*p* emission line, combined with the thickness measurement by TEM. The

basic pressure of this ultrahigh vacuum system was less than  $5 \times 10^{-10}$  torr. Moreover, no other elemental contamination needed to be considered during the growth and *in situ* measurement process, from which the evolution of the electronic structure was recorded from the substrate to the overlayer. In addition, the structure of the NiO film as well as the epitaxial relationship between the NiO overlayer and ZnO substrate were characterized by *ex situ* synchrotron-based XRD (theta-2 theta and phi scan) with  $\lambda = 0.514$  nm. STEM imaging and EELS measurements at the interface of NiO(001)/ZnO(0001) were performed using a double aberration-corrected JEOL-ARM200CF microscope with a cold-field emission gun operated at 200 kV. The microscope was equipped with JEOL and Gatan HAADF detectors for incoherent HAADF (*Z* contrast) imaging and a Gatan GIF Quantum ER energy filter with dual EELS for EELS. High-resolution TEM images were examined using a JEOL2100F instrument. The focused ion beam (FIB) *in situ* lift-out technique was used to prepare the TEM thin-film samples.

## VI. COMPUTATIONAL DETAILS

The theoretical calculations were performed using the Quantum ESPRESSO package [62]. Ultrasoft pseudopotentials [63] were used, and the exchange correlation was described by the local-density approximation functional [64]. To correctly reproduce the electronic structures of the Ni-3*d* states, the spin-polarized local-density approximation (LDA + *U*) method was used, and the on-site Coulomb term *U* was chosen to be 7.6 eV [65]. The kinetic-energy cutoff of plane waves was set at 55 Ry. The mesh for *k*-point sampling was  $2 \times 3 \times 1$  for the superlattice models. The atomic positions were fully relaxed until the force on every atom was less than 0.01 eV/Å. The stacking direction in the superlattice models was along the *z* direction, hence only the lattice constant *c* was fully relaxed.

## ACKNOWLEDGMENTS

This work was supported by the National Natural Science Foundation of China (Grants No. U1332105 and No. 11704317) and by the Xiamen University Malaysia Research Fund (Grant No. XMUMRF/2019-C4/IORI/0002). HRTEM/STEM work at the Condensed Matter Physics and Materials Science Department and the Center for Functional Nanomaterials was supported by the U.S. Department of Energy, Office of Basic Energy Science, Division of Materials Science and Engineering, under Contract No. DE-SC0012704. The authors thank C. Liu, J. Zhao, J. Li, and B. Gao for their assistance with the synchrotron-based experiments.

- 
- [1] V. Sushmitha, V. Maragatham, P. D. Raj, and M. Sridharan, Structural, electrical, optical and magnetic properties of NiO/ZnO thin films, *IOP Conf. Ser.: Mater. Sci. Eng.* **310**, 012022 (2018).  
 [2] A. Bera, H. Peng, J. Lourembam, Y. Shen, X. W. Sun, and T. Wu, A versatile light-switchable nanorod memory: wurtzite zno on perovskite SrTiO<sub>3</sub>, *Adv. Funct. Mater.* **23**, 4977 (2013).

- [3] M. Brandt, H. Frenzel, H. Hochmuth, M. Lorenz, M. Grundmann, and J. Schubert, Ferroelectric thin film field-effect transistors based on ZnO/BaTiO<sub>3</sub> heterostructures, *J. Vac. Sci. Technol., B: Microelectron. Nanometer Struct.–Process., Meas., Phenom.* **27**, 1789 (2009).  
 [4] O. Game, U. Singh, T. Kumari, A. Banpurkar, and S. Ogale, ZnO (N)-Spiro-MeOTAD hybrid photodiode: an efficient

- self-powered fast-response UV (visible) photosensor, *Nanoscale* **6**, 503 (2014).
- [5] Y. Li, H.-Q. Wang, H. Zhou, D. Du, W. Geng, D. Lin, X. Chen, H. Zhan, Y. Zhou, and J. Kang, Tuning the surface morphologies and properties of ZnO films by the design of interfacial layer, *Nanoscale Res. Lett.* **12**, 551 (2017).
  - [6] H. Zhou, L. Wu, H.-Q. Wang, J.-C. Zheng, L. Zhang, K. Kisslinger, Y. Li, Z. Wang, H. Cheng, S. Ke, Y. Li, J. Kang, and Y. Zhu, Interfaces between hexagonal and cubic oxides and their structure alternatives, *Nat. Commun.* **8**, 1474 (2017).
  - [7] P. Waltereit, O. Brandt, A. Trampert, H. Grahn, J. Menniger, M. Ramsteiner, M. Reiche, and K. Ploog, Nitride semiconductors free of electrostatic fields for efficient white light-emitting diodes, *Nature (London)* **406**, 865 (2000).
  - [8] X. L. Du, Z. X. Mei, Z. L. Liu, Y. Guo, T. C. Zhang, Y. N. Hou, Z. Zhang, Q. K. Xue, and A. Y. Kuznetsov, Controlled growth of high-quality ZnO-based films and fabrication of visible-blind and solar-blind ultra-violet detectors, *Adv. Mater.* **21**, 4625 (2009).
  - [9] S. J. Pearton and F. Ren, Advances in ZnO-based materials for light emitting diodes, *Curr. Opin. Chem. Eng.* **3**, 51 (2014).
  - [10] H. Long, S. Z. Li, X. M. Mo, H. N. Wang, H. H. Huang, Z. Chen, Y. P. Liu, and G. J. Fang, Electroluminescence from ZnO-nanorod-based double heterostructured light-emitting diodes, *Appl. Phys. Lett.* **103**, 123504 (2013).
  - [11] N. Zhang, K. Yu, Q. Li, C. Q. Song, L. Zhu, and Z. Q. Zhu, Room-temperature blue-violet laser emission from individual ultra-long ZnO microbelts, *Mater. Lett.* **121**, 231 (2014).
  - [12] Y. Nakano, T. Morikawa, T. Ohwaki, and Y. Taga, Electrical characterization of p-type N-doped ZnO films prepared by thermal oxidation of sputtered Zn<sub>3</sub>N<sub>2</sub> films, *Appl. Phys. Lett.* **88**, 172103 (2006).
  - [13] D. C. Look, K. D. Leedy, L. Vines, B. G. Svensson, A. Zubiaga, F. Tuomisto, D. R. Doust, and L. J. Brillson, Self-compensation in semiconductors: the Zn vacancy in Ga-doped ZnO, *Phys. Rev. B* **84**, 115202 (2011).
  - [14] H. Ohta, M. Hirano, K. Nakahara, H. Maruta, T. Tanabe, M. Kamiya, T. Kamiya, and H. Hosono, Fabrication and photoresponse of a pn-heterojunction diode composed of transparent oxide semiconductors, p-NiO and n-ZnO, *Appl. Phys. Lett.* **83**, 1029 (2003).
  - [15] Y. Vygranenko, K. Wang, and A. Nathan, Low leakage p-NiO/i-ZnO/n-ITO heterostructure ultraviolet sensor, *Appl. Phys. Lett.* **89**, 172105 (2006).
  - [16] Y. Y. Xi, Y. F. Hsu, A. B. Djurisic, A. M. C. Ng, W. K. Chan, H. L. Tam, and K. W. Cheah, NiO/ZnO light emitting diodes by solution-based growth, *Appl. Phys. Lett.* **92**, 113505 (2008).
  - [17] S. Y. Tsai, M. H. Hon, and Y. M. Lu, Fabrication of transparent p-NiO/n-ZnO heterojunction devices for ultraviolet photodetectors, *Solid-State Electron.* **63**, 37 (2011).
  - [18] M. R. Hasan, T. Xie, S. C. Barron, G. N. Liu, N. V. Nguyen, A. Motayed, M. V. Rao, and R. Debnath, Self-powered p-NiO/n-ZnO heterojunction ultraviolet photodetectors fabricated on plastic substrates, *APL Mater.* **3**, 106101 (2015).
  - [19] Z. G. Yang, L. P. Zhu, Y. M. Guo, W. Tian, Z. Z. Ye, and B. H. Zhao, Valence-band offset of p-NiO/n-ZnO heterojunction measured by X-ray photoelectron spectroscopy, *Phys. Lett. A* **375**, 1760 (2011).
  - [20] M. J. Ma, B. Lu, T. T. Zhou, Z. Z. Ye, J. G. Lu, and X. H. Pan, Orientation dependent band alignment for p-NiO/n-ZnO heterojunctions, *J. Appl. Phys.* **113**, 163704 (2013).
  - [21] T. A. Dar, A. Agrawal, P. Misra, L. M. Kukreja, P. K. Sen, and P. Sen, Valence and conduction band offset measurements in Ni<sub>0.07</sub>Zn<sub>0.93</sub>O/ZnO heterostructure, *Curr. Appl. Phys.* **14**, 171 (2014).
  - [22] R. B. Comes, S. R. Spurgeon, S. M. Heald, D. M. Kepaptsoglou, L. Jones, P. V. Ong, M. E. Bowden, Q. M. Ramasse, P. V. Sushko, and S. A. Chambers, Interface-Induced Polarization in SrTiO<sub>3</sub>-LaCrO<sub>3</sub> Superlattices, *Adv. Mater. Interfaces* **3**, 1500779 (2016).
  - [23] Y. Zhang, N. Lin, Y. Li, X. Wang, H. Wang, J. Kang, R. Wilks, M. Bär, and R. Mu, The isotype ZnO/SiC heterojunction prepared by molecular beam epitaxy—A chemical inert interface with significant band discontinuities, *Sci. Rep.* **6**, 23106 (2016).
  - [24] H. Q. Wang, W. W. Gao, E. I. Altman, and V. E. Henrich, Studies of the electronic structure at the Fe<sub>3</sub>O<sub>4</sub>-NiO interface, *J. Vac. Sci. Technol. A* **22**, 1675 (2004).
  - [25] C. Chen, L. Tjeng, J. Kwo, H. Kao, P. Rudolf, F. Sette, and R. Fleming, Out-of-Plane Orbital Characters of Intrinsic and Doped Holes in La<sub>2-x</sub>Sr<sub>x</sub>CuO<sub>4</sub>, *Phys. Rev. Lett.* **68**, 2543 (1992).
  - [26] M. Haverkort, S. Csiszar, Z. Hu, S. Altieri, A. Tanaka, H. Hsieh, H.-J. Lin, C. Chen, T. Hibma, and L. Tjeng, Magnetic versus crystal-field linear dichroism in NiO thin films, *Phys. Rev. B* **69**, 020408(R) (2004).
  - [27] H. Guo, J.-O. Wang, X. He, Z. Yang, Q. Zhang, K.-J. Jin, C. Ge, R. Zhao, L. Gu, Y. Feng, W. Zhou, X. Li, Q. Wan, M. He, C. Hong, Z. Guo, C. Wang, H. Lu, K. Ibrahim, and S. Meng *et al.*, The origin of oxygen vacancies controlling La<sub>2/3</sub>Sr<sub>1/3</sub>MnO<sub>3</sub> electronic and magnetic properties, *Adv. Mater. Interfaces* **3**, 1500753 (2016).
  - [28] A. B. Shah, Q. M. Ramasse, X. Zhai, J. G. Wen, S. J. May, I. Petrov, A. Bhattacharya, P. Abbamonte, J. N. Eckstein, and J. M. Zuo, Probing interfacial electronic structures in atomic layer LaMnO<sub>3</sub> and SrTiO<sub>3</sub> superlattices, *Adv. Mater.* **22**, 1156 (2010).
  - [29] C. Wang, K.-J. Jin, L. Gu, H.-B. Lu, S.-M. Li, W.-J. Zhou, R.-Q. Zhao, H.-Z. Guo, M. He, and G.-Z. Yang, Crucial role played by interface and oxygen content in magnetic properties of ultrathin manganite films, *Appl. Phys. Lett.* **102**, 252401 (2013).
  - [30] S. A. Chambers, M. H. Engelhard, V. Shutthanandan, Z. Zhu, T. C. Droubay, L. Qiao, P. Sushko, T. Feng, H. D. Lee, and T. Gustafsson, Instability, intermixing and electronic structure at the epitaxial LaAlO<sub>3</sub>/SrTiO<sub>3</sub> (001) heterojunction, *Surf. Sci. Rep.* **65**, 317 (2010).
  - [31] K. Song, H. Schmid, V. Srot, E. Gilardi, G. Gregori, K. Du, J. Maier, and P. A. van Aken, Cerium reduction at the interface between ceria and yttria-stabilised zirconia and implications for interfacial oxygen non-stoichiometry, *APL Mater.* **2**, 032104 (2014).
  - [32] S. J. Pennycook, H. Zhou, M. F. Chisholm, A. Y. Borisevich, M. Varela, J. Gazquez, T. J. Pennycook, and J. Narayan, Misfit accommodation in oxide thin film heterostructures, *Acta Mater.* **61**, 2725 (2013).
  - [33] L. Hong, K. Bhatnagar, R. Droopad, R. F. Klie, and S. Ögüt, Atomic-scale structural and electronic properties of SrTiO<sub>3</sub>/GaAs interfaces: A combined STEM-EELS and first-principles study, *Phys. Rev. B* **96**, 035311 (2017).

- [34] S. Middey, P. Rivero, D. Meyers, M. Kareev, X. Liu, Y. Cao, J. W. Freeland, S. Barraza-Lopez, and J. Chakhalian, Polarity compensation in ultra-thin films of complex oxides: the case of a perovskite nickelate, *Sci. Rep.* **4**, 6819 (2014).
- [35] M. N. Grisolia, J. Varignon, G. Sanchez-Santolino, A. Arora, S. Valencia, M. Varela, R. Abrudan, E. Weschke, E. Schierle, J. E. Rault, J. P. Rueff, A. Barthelemy, J. Santamaria, and M. Bibes, Hybridization-controlled charge transfer and induced magnetism at correlated oxide interfaces, *Nat. Phys.* **12**, 484 (2016).
- [36] M. Grundmann, T. Bontgen, and M. Lorenz, Occurrence of Rotation Domains in Heteroepitaxy, *Phys. Rev. Lett.* **105**, 146102 (2010).
- [37] See Supplemental Material at <http://link.aps.org/supplemental/10.1103/PhysRevMaterials.4.124601> for low magnification TEM image, comparison between experimental STEM-HAADF images, the fitting equation for EELS spectra and examples for multiple linear least square fitting.
- [38] V. J. Keast, A. J. Scott, R. Brydson, D. B. Williams, and J. Bruley, Electron energy-loss near-edge structure - a tool for the investigation of electronic structure on the nanometre scale, *J. Microsc.* **203**, 135 (2001).
- [39] Y. Koyama, T. Mizoguchi, H. Ikeno, and I. Tanaka, Electronic structure of lithium nickel oxides by electron energy loss spectroscopy, *J. Phys. Chem. B* **109**, 10749 (2005).
- [40] D. Alders, L. H. Tjeng, F. C. Voegt, T. Hibma, G. A. Sawatzky, C. T. Chen, J. Vogel, M. Sacchi, and S. Iacobucci, Temperature and thickness dependence of magnetic moments in NiO epitaxial films, *Phys. Rev. B* **57**, 11623 (1998).
- [41] H. Wang, P. Ge, C. Riordan, S. Brooker, C. Woomer, T. Collins, C. Melendres, O. Graudejus, N. Bartlett, and S. Cramer, Integrated X-ray L absorption spectra. Counting holes in Ni complexes, *J. Phys. Chem. B* **102**, 8343 (1998).
- [42] R. J. Woolley, B. N. Illy, M. P. Ryan, and S. J. Skinner, In situ determination of the nickel oxidation state in  $\text{La}_2\text{NiO}_{4+\delta}$  and  $\text{La}_4\text{Ni}_3\text{O}_{10-\delta}$  using X-ray absorption near-edge structure, *J. Mater. Chem.* **21**, 18592 (2011).
- [43] G. Sawatzky and J. Allen, Magnitude and Origin of the Band Gap in NiO, *Phys. Rev. Lett.* **53**, 2339 (1984).
- [44] A. Fujimori, F. Minami, and S. Sugano, Multielectron satellites and spin polarization in photoemission from Ni compounds, *Phys. Rev. B* **29**, 5225 (1984).
- [45] H. Ikeno, I. Tanaka, Y. Koyama, T. Mizoguchi, and K. Ogasawara, First-principles multielectron calculations of Ni  $L_{2,3}$  NEXAFS and ELNES for  $\text{LiNiO}_2$  and related compounds, *Phys. Rev. B* **72**, 075123 (2005).
- [46] J. Chakhalian, J. Rondinelli, J. Liu, B. Gray, M. Kareev, E. Moon, N. Prasai, J. Cohn, M. Varela, and I.-C. Tung, Asymmetric Orbital-Lattice Interactions in Ultrathin Correlated Oxide Films, *Phys. Rev. Lett.* **107**, 116805 (2011).
- [47] I. Preda, M. Abbate, A. Gutiérrez, S. Palacín, A. Vollmer, and L. Soriano, Study of the growth of NiO on highly oriented pyrolytic graphite by X-ray absorption spectroscopy, *J. Electron Spectrosc. Relat. Phenom.* **156-158**, 111 (2007).
- [48] S. Tanuma, C. J. Powell, and D. R. Penn, Calculations of electron inelastic mean free paths (IMFPs). IV. Evaluation of calculated IMFPs and of the predictive IMFP formula TPP-2 for electron energies between 50 and 2000 eV, *Surf. Interface Anal.* **20**, 77 (1993).
- [49] S. Tougaard, QUASES-IMFP-TPP2M Ver 2.2. QUASES-IMFP-TPP2M. <http://www.quases.com/> (2002).
- [50] M. Nakamura, Y. Takata, and N. Kosugi, Resonant Ni 3p and 3s photoemission for the Ni 2p core-excitation in NiO, *J. Electron Spectrosc. Relat. Phenom.* **78**, 115 (1996).
- [51] P. S. Bagus, E. S. Ilton, and C. J. Nelin, The interpretation of XPS spectra: Insights into materials properties, *Surf. Sci. Rep.* **68**, 273 (2013).
- [52] M. A. Vanveenendaal and G. A. Sawatzky, Nonlocal Screening Effects in 2p X-Ray Photoemission Spectroscopy Core-Level Line Shapes of Transition Metal Compounds, *Phys. Rev. Lett.* **70**, 2459 (1993).
- [53] P. S. Bagus, F. Illas, G. Pacchioni, and F. Parmigiani, Mechanisms responsible for chemical shifts of core-level binding energies and their relationship to chemical bonding, *J. Electron Spectrosc. Relat. Phenom.* **100**, 215 (1999).
- [54] X. M. Li, Z. M. Zhang, and V. E. Henrich, Inelastic electron background function for ultraviolet photoelectron spectra, *J. Electron Spectrosc. Relat. Phenom.* **63**, 253 (1993).
- [55] H. Q. Wang, E. I. Altman, and V. E. Henrich, Measurement of electronic structure at nanoscale solid-solid interfaces by surface-sensitive electron spectroscopy, *Appl. Phys. Lett.* **92**, 012118 (2008).
- [56] H. Q. Wang, E. Altman, C. Broadbridge, Y. M. Zhu, and V. Henrich, Determination of electronic structure of oxide-oxide interfaces by photoemission spectroscopy, *Adv. Mater.* **22**, 2950 (2010).
- [57] Z. X. Shen, R. S. List, D. S. Dessau, B. O. Wells, O. Jepsen, A. J. Arko, R. Bartlett, C. K. Shih, F. Parmigiani, J. C. Huang, and P. A. P. Lindberg, Electronic structure of NiO: Correlation and band effects, *Phys. Rev. B* **44**, 3604 (1991).
- [58] J. Kunes, V. I. Anisimov, S. L. Skornyakov, A. V. Lukoyanov, and D. Vollhardt, NiO: Correlated Band Structure of a Charge-Transfer Insulator, *Phys. Rev. Lett.* **99**, 156404 (2007).
- [59] Q. Yin, A. Gordienko, X. G. Wan, and S. Y. Savrasov, Calculated Momentum Dependence of Zhang-Rice States in Transition Metal Oxides, *Phys. Rev. Lett.* **100**, 066406 (2008).
- [60] M. Taguchi, M. Matsunami, Y. Ishida, R. Eguchi, A. Chainani, Y. Takata, M. Yabashi, K. Tamasaku, Y. Nishino, T. Ishikawa, Y. Senba, H. Ohashi, and S. Shin, Revisiting the Valence-Band and Core-Level Photoemission Spectra of NiO, *Phys. Rev. Lett.* **100**, 206401 (2008).
- [61] R. J. O. Mossaneck, I. Preda, M. Abbate, J. Rubio-Zuazo, G. R. Castro, A. Vollmer, A. Gutierrez, and L. Soriano, Investigation of surface and non-local screening effects in the Ni 2p core level photoemission spectra of NiO, *Chem. Phys. Lett.* **501**, 437 (2011).
- [62] P. Giannozzi, S. Baroni, N. Bonini, M. Calandra, R. Car, C. Cavazzoni, D. Ceresoli, G. L. Chiarotti, M. Cococcioni, and I. Dabo, Quantum espresso: a modular and open-source software project for quantum simulations of materials, *J. Phys.: Condens. Matter* **21**, 395502 (2009).
- [63] D. Vanderbilt, Soft self-consistent pseudopotentials in a generalized eigenvalue formalism, *Phys. Rev. B* **41**, 7892 (1990).
- [64] A. D. Becke, A new mixing of Hartree-Fock and local density-functional theories, *J. Chem. Phys.* **98**, 1372 (1993).
- [65] C. Gougoussis, M. Calandra, A. Seitsonen, C. Brouder, A. Shukla, and F. Mauri, Intrinsic charge transfer gap in NiO from Ni K-edge x-ray absorption spectroscopy, *Phys. Rev. B* **79**, 045118 (2009).